

OzDES multifibre spectroscopy for the Dark Energy Survey: Three year results and first data release

M. J. Childress¹, C. Lidman^{2,3}, T. M. Davis^{4,3}, B. E. Tucker^{5,3}, J. Asorey^{4,3}, F. Yuan^{3,5}, T. M. C. Abbott⁶, F. B. Abdalla^{7,8}, S. Allam⁹, J. Annis⁹, M. Banerji^{10,11}, A. Benoit-Lévy^{12,7,13}, S. .R. Bernard^{14,3}, E. Bertin^{12,13}, D. Brooks⁷, E. Buckley-Geer⁹, D. L. Burke^{15,16}, A. Carnero Rosell^{17,18}, D. Carollo^{3,19}, M. Carrasco Kind^{20,21}, J. Carretero²², F. J. Castander⁹, C. E. Cunha¹⁵, L. N. da Costa^{17,18}, C. B. D'Andrea²⁴, P. Doel⁷, T. F. Eifler^{25,26}, A. E. Evrard^{27,28}, B. Flaugher⁹, R. J. Foley²⁹, P. Fosalba²³, J. Frieman^{9,30}, J. García-Bellido³¹, K. Glazebrook³², D. A. Goldstein^{33,34}, D. Gruen^{15,16}, R. A. Gruendl^{20,21}, J. Gschwend^{17,18}, R. R. Gupta³⁵, G. Gutierrez⁹, S.R. Hinton^{4,3}, J. K. Hoormann⁴, D. J. James^{36,6}, R. Kessler³⁰, A. G. Kim³⁴, A. L. King^{3,4}, E. Kovacs³⁵, K. Kuehn², S. Kuhlmann³⁵, N. Kuropatkin⁹, D. J. Lagattuta³⁷, G. F. Lewis³⁸, T. S. Li^{9,39}, M. Lima^{40,17}, H. Lin⁹, E. Macaulay⁴¹, M. A. G. Maia^{17,18}, J. Marriner⁹, M. March²⁴, J. L. Marshall³⁹, P. Martini^{42,43}, R. G. McMahon^{10,11}, F. Menanteau^{20,21}, R. Miquel^{44,22}, A. Moller^{3,5}, E. Morganson²¹, J. Mould³², D. Mudd⁴³, D. Muthukrishna^{4,3,5}, R. C. Nichol⁴¹, B. Nord⁹, R. L. C. Ogando^{17,18}, F. Ostrovski^{10,45}, D. Parkinson^{4,3}, A. A. Plazas²⁶, S. L. Reed^{10,11}, K. Reil¹⁶, A. K. Romer⁴⁶, E. S. Rykoff^{15,16}, M. Sako²⁴, E. Sanchez⁴⁷, V. Scarpine⁹, R. Schindler¹⁶, M. Schubnell²⁸, D. Scolnic³⁰, I. Sevilla-Noarbe⁴⁷, N. Seymour⁴⁸, R. Sharp⁵, M. Smith¹, M. Soares-Santos⁹, F. Sobreira^{49,17}, N. E. Sommer^{5,3}, H. Spinka³⁵, E. Suchyta⁵⁰, M. Sullivan¹, M. E. C. Swanson²¹, G. Tarle²⁸, S. A. Uddin^{51,3}, A. R. Walker⁶, W. Wester⁹, B. R. Zhang^{3,5}

(DES Collaboration)

¹ School of Physics and Astronomy, University of Southampton, Southampton, SO17 1BJ, UK

² Australian Astronomical Observatory, 105 Delhi Road, North Ryde, NSW 2113, Australia

³ ARC Centre of Excellence for All-sky Astrophysics (CAASTRO)

⁴ School of Mathematics and Physics, University of Queensland, Brisbane, QLD 4072, Australia

⁵ The Research School of Astronomy and Astrophysics, Australian National University, ACT 2601, Australia

⁶ Cerro Tololo Inter-American Observatory, National Optical Astronomy Observatory, Casilla 603, La Serena, Chile

⁷ Department of Physics & Astronomy, University College London, Gower Street, London, WC1E 6BT, UK

⁸ Department of Physics and Electronics, Rhodes University, PO Box 94, Grahamstown, 6140, South Africa

⁹ Fermi National Accelerator Laboratory, P. O. Box 500, Batavia, IL 60510, USA

¹⁰ Institute of Astronomy, University of Cambridge, Madingley Road, Cambridge CB3 0HA, UK

¹¹ Kavli Institute for Cosmology, University of Cambridge, Madingley Road, Cambridge CB3 0HA, UK

¹² CNRS, UMR 7095, Institut d'Astrophysique de Paris, F-75014, Paris, France

¹³ Sorbonne Universités, UPMC Univ Paris 06, UMR 7095, Institut d'Astrophysique de Paris, F-75014, Paris, France

¹⁴ School of Physics, The University of Melbourne, Parkville, VIC 3010, Australia

¹⁵ Kavli Institute for Particle Astrophysics & Cosmology, P. O. Box 2450, Stanford University, Stanford, CA 94305, USA

¹⁶ SLAC National Accelerator Laboratory, Menlo Park, CA 94025, USA

¹⁷ Laboratório Interinstitucional de e-Astronomia - LIneA, Rua Gal. José Cristino 77, Rio de Janeiro, RJ - 20921-400, Brazil

¹⁸ Observatório Nacional, Rua Gal. José Cristino 77, Rio de Janeiro, RJ - 20921-400, Brazil

¹⁹ INAF - Osservatorio Astronomico di Torino, 10025, Italy

²⁰ Department of Astronomy, University of Illinois, 1002 W. Green Street, Urbana, IL 61801, USA

²¹ National Center for Supercomputing Applications, 1205 West Clark St., Urbana, IL 61801, USA

²² Institut de Física d'Altes Energies (IFAE), The Barcelona Institute of Science and Technology, Campus UAB, 08193 Bellaterra (Barcelona) Spain

²³ Institut de Ciències de l'Espai, IEEC-CSIC, Campus UAB, Carrer de Can Magrans, s/n, 08193 Bellaterra, Barcelona, Spain

²⁴ Department of Physics and Astronomy, University of Pennsylvania, Philadelphia, PA 19104, USA

²⁵ Department of Physics, California Institute of Technology, Pasadena, CA 91125, USA

²⁶ Jet Propulsion Laboratory, California Institute of Technology, 4800 Oak Grove Dr., Pasadena, CA 91109, USA

²⁷ Department of Astronomy, University of Michigan, Ann Arbor, MI 48109, USA

²⁸ Department of Physics, University of Michigan, Ann Arbor, MI 48109, USA

²⁹ Department of Astronomy and Astrophysics, University of California, Santa Cruz, CA 95064, USA

³⁰ Kavli Institute for Cosmological Physics, University of Chicago, Chicago, IL 60637, USA

³¹ Instituto de Física Teórica UAM/CSIC, Universidad Autónoma de Madrid, 28049 Madrid, Spain

³² Centre for Astrophysics & Supercomputing, Swinburne University of Technology, Victoria 3122, Australia

³³ Department of Astronomy, University of California, Berkeley, 501 Campbell Hall, Berkeley, CA 94720, USA

³⁴ Lawrence Berkeley National Laboratory, 1 Cyclotron Road, Berkeley, CA 94720, USA

³⁵ Argonne National Laboratory, 9700 South Cass Avenue, Lemont, IL 60439, USA

³⁶ Astronomy Department, University of Washington, Box 351580, Seattle, WA 98195, USA

³⁷ Univ Lyon, Univ Lyon1, Ens de Lyon, CNRS, Centre de Recherche Astrophysique de Lyon UMR5574, F-69230, Saint-Genis-Laval, France

³⁸ Sydney Institute for Astronomy, School of Physics, A28, The University of Sydney, NSW 2006, Australia

³⁹ George P. and Cynthia Woods Mitchell Institute for Fundamental Physics and Astronomy, and Department of Physics and Astronomy, Texas A&M University, College Station, TX 77843, USA

⁴⁰ Departamento de Física Matemática, Instituto de Física, Universidade de São Paulo, CP 66318, CEP 05314-970, São Paulo, SP, Brazil

⁴¹ Institute of Cosmology & Gravitation, University of Portsmouth, Portsmouth, PO1 3FX, UK

⁴² Center for Cosmology and Astro-Particle Physics, The Ohio State University, Columbus, OH 43210, USA

⁴³ Department of Astronomy, The Ohio State University, Columbus, OH 43210, USA

⁴⁴ Institució Catalana de Recerca i Estudis Avançats, E-08010 Barcelona, Spain

⁴⁵ Departamento de Astronomia, Instituto de Física da Universidade Federal do Rio Grande do Sul, 91501-970, Porto Alegre, Brazil

⁴⁶ Department of Physics and Astronomy, Pevensey Building, University of Sussex, Brighton, BN1 9QH, UK

⁴⁷ Centro de Investigaciones Energéticas, Medioambientales y Tecnológicas (CIEMAT), Madrid, Spain

⁴⁸ International Centre for Radio Astronomy Research, Curtin University, Perth, Australia

⁴⁹ Instituto de Física Gleb Wataghin, Universidade Estadual de Campinas, 13083-859, Campinas, SP, Brazil

⁵⁰ Computer Science and Mathematics Division, Oak Ridge National Laboratory, Oak Ridge, TN 37831

⁵¹ Purple Mountain Observatory, Chinese Academy of Sciences

ABSTRACT

We present results for the first three years of OzDES, a six-year program to obtain redshifts for objects in the Dark Energy Survey (DES) supernova fields using the 2dF fibre positioner and AAOmega spectrograph on the Anglo-Australian Telescope. OzDES is a multi-object spectroscopic survey targeting multiple types of targets at multiple epochs over a multi-year baseline, and is one of the first multi-object spectroscopic surveys to dynamically include transients into the target list soon after their discovery. At the end of three years, OzDES has spectroscopically confirmed almost 100 supernovae, and has measured redshifts for 17,000 objects, including the redshifts of 2,566 supernova hosts. We examine how our ability to measure redshifts for targets of various types depends on signal-to-noise, magnitude, and exposure time, finding that our redshift success rate increases significantly at a signal-to-noise of 2 to 3 per 1-Ångstrom bin. We also find that the change in signal-to-noise with exposure time closely matches the Poisson limit for stacked exposures as long as 10 hours. We use these results to predict the redshift yield of the full OzDES survey, as well as the potential yields of future surveys on other facilities such as 4MOST, PFS, and MSE. This work marks the first OzDES data release, comprising 14,693 redshifts. OzDES is on target to obtain over 30,000 redshifts over the six-year duration of the survey, including a yield of approximately 5,700 supernova host-galaxy redshifts.

Key words: cosmology: dark energy; supernovae: general

1 INTRODUCTION

Wide-field, multi-object spectroscopy (MOS) has revolutionized our understanding of cosmology, galaxy evolution and Galactic structure. Historically, most large MOS campaigns have used target lists that are defined well in advance of the MOS observing campaign. Examples include galaxy redshift surveys that are designed to measure large scale structure, such as SDSS (York et al. 2000), 2dFGRS (Colless et al. 2001), 2SLAQ (Cannon et al. 2006), WiggleZ (Drinkwater et al. 2010), BOSS (Dawson et al. 2013), VIPERS (Scodeggio et al. 2016) and 2dFLenS (Blake et al. 2016); galaxy surveys that are designed to measure the detailed physical properties of galaxies, such as SDSS (York et al. 2000) and GAMA (Driver et al. 2011); and surveys that are designed to trace the build-up of stellar mass in the Galaxy, such as the GALAH survey (De Silva et al. 2015).

In the modern era of large surveys, this observing strategy is being supplemented by ones that incorporate *dynamic* target selection. In these surveys, target selection is done shortly before the observation, thus allowing transients to be observed soon after they are discovered. This model for MOS surveys is being pioneered by the OzDES survey (Yuan et al. 2015), which is obtaining spectra and redshifts for the Dark Energy Survey (DES; Flaugher 2005). Such a strategy will become standard for future facilities with large, rapidly reconfigurable fiber positioners, such as 4MOST (de Jong et al. 2012), the Subaru Prime Focus Spectrograph (PFS; Sugai et al. 2012; Takada et al. 2014), the Dark Energy Spectroscopic Instrument (Aghamousa et al. 2016), and the Mauna Kea Spectroscopic Explorer (MSE; Simons et al. 2014; McConnachie et al. 2014), all of which will conduct numerous parallel spectroscopic programs including some related to dynamic targets discovered by LSST (Tyson 2002; LSST Science Collaboration et al. 2009a).

This paper presents results from the first three years of the OzDES survey, and describes the first OzDES data release. The detailed survey description and results from the first year are presented in Yuan et al. (2015). Briefly, the science objectives of OzDES include obtaining supernova (SN) host-galaxy redshifts for cosmology (e.g., Bazin et al. 2011; Campbell et al. 2013), spectroscopically classifying active transients, monitoring a sample of active galactic nuclei (AGN) for reverberation mapping (RM – see e.g., Bentz et al. 2009; King et al. 2015) and potentially for cosmology (Watson et al. 2011; King et al. 2014), securing redshifts for a wide variety of galaxies to be used for photometric redshift training (e.g., Sánchez et al. 2014; Bonnett et al. 2016), including a large sample of luminous red galaxies (LRGs; Banerji et al. 2015), and using redshifts of selected galaxies to confirm their membership in clusters (e.g., Rozo et al. 2016; Rykoff et al. 2016). OzDES has already produced several discoveries, including spectroscopy of hundreds of active transients, many new QSOs (Tie et al. 2017), and the first FeLoBAL QSO in a post-starburst galaxy (Mudd et al. 2016).

Here we focus on the main outcomes from the first three years of observations, which have comprised just over half of the allocated observing time for OzDES. This paper also marks the first public release of redshifts secured by OzDES, which consists of 14,693 redshifts from a wide variety of target classes (we note the SN host-galaxy redshifts will be released in conjunction with future DES supernova analyses). We anticipate future data releases from OzDES to include a final redshift catalogue to be released shortly after the conclusion of the survey, and an anticipated final release including the OzDES spectra some time after that.

This paper is organised as follows: Section 2 presents the operational details for the second and third years of OzDES observations, including a full accounting of fibre allocation. Section 3 describes the redshift success rates for OzDES for various target types as a function of magnitude and spectrum signal-to-noise. The first OzDES data release is then described in Section 4. In Section 5, we examine how signal-to-noise depends on exposure time, and in Section 6, we discuss the prospects for the full OzDES survey and future multi-object spectroscopy surveys. Finally, we present concluding remarks in Section 7.

This paper is organised as follows: Section 2 presents the operational details for the second and third years of OzDES observations, including a full accounting of fibre allocation. Section 3 describes the redshift success rates for OzDES for various target types as a function of magnitude and spectrum signal-to-noise. The first OzDES data release is then described in Section 4. In Section 5, we examine how signal-to-noise depends on exposure time, and in Section 6, we discuss the prospects for the full OzDES survey and future multi-object spectroscopy surveys. Finally, we present concluding remarks in Section 7.

2 OZDES OPERATIONS FOR YEARS 2 AND 3

In this Section, we describe several key aspects of the operational strategy for the second and third years of OzDES observing (the

analogous information for first year operations was presented in Yuan et al. 2015). Section 2.1 describes the instrument setup, calibration strategy, and general observing log. Section 2.2 describes the data reduction procedures, with a particular emphasis on upgrades from the first year of OzDES operations. Finally, Section 2.3 presents the allocation of 2dF fibres to the various OzDES target types.

Throughout this paper we will use the notation Y1/Y2/Y3 to denote the first/second/third years of OzDES operations, respectively. Y1 corresponds to semester B of 2013 (i.e. August 2013 to January 2014) and includes data that were taken during a couple of science verification runs at the end semester B in 2012, Y2 to semester B of 2014, and Y3 to semester B of 2015. These correspond to the same operational years for the Dark Energy Survey (DES).

2.1 Instrument Setup and Calibration Strategy

OzDES utilises the AAOmega spectrograph with the 2dF robotic fibre positioner on the 3.9-metre Anglo-Australian Telescope (AAT) at Siding Spring Observatory in Australia to target the 10 DES supernova fields, which cover a total area of 27 sq. degrees. The coordinates of the fields are listed in Table 1 of Yuan et al. (2015).

AAOmega consists of red and blue arms that are split by a dichroic. We used the x5700 dichroic, which splits the arms at 5700 Å. In the blue arm, we used the 580V grating centred at 4800 Å in Y1 and Y2, but in Y3 we shifted the central wavelength by 20 Å to 4820 Å to provide larger overlap between the red and blue arms of the spectrograph. In the red arm, we used the 385R grating centred at 7250 Å. This setup provides continuous wavelength coverage from ~ 3700 Å to ~ 8800 Å. The overlap between the red and blue arms is typically ~ 40 Å (~ 60 Å for Y3), although this depends on fibre location due to the different spectral curvature of the red and blue gratings.

The 2dF robotic positioner can place up to 392 science fibres and 8 guide fibres within a 2.1 degree diameter patrol field. The patrol field of 2dF matches closely the field of view of the DECam imager (Flaugher et al. 2015) on the CTIO 4m Blanco telescope (see Fig. 1 in Yuan et al. 2015).

Between Y1 and Y2, the CCDs in the red and blue arms of AAOmega were replaced. The new CCD in the blue arm has superior quantum efficiency and has far fewer cosmetic defects (Brough et al. 2014). Bias and dark frames are used to remove these defects in the old CCD, but these frames are no longer needed for the new CCD (though we continue to take a set of dark and bias frames during each observing run to confirm this). The new CCD in the red arm is thicker than the previous one, and has less fringing at redder wavelengths. The thicker CCD also has higher quantum efficiency than the older CCD, especially beyond ~ 8800 Å, but is affected more by cosmic rays.

The AAOmega data calibration strategy for Y1 of OzDES is described in Yuan et al. (2015). Beginning in Y2, we made a number of changes. In addition to taking flat fields using the flaps that fold in front of the 2dF corrector (called flap flats), we took flat fields using an illuminated section of the dome wind-screen (called dome flats). Dome flats were taken once per run for each plate¹,

¹ 2dF consists of two plates. While one plate is being observed, the other plate is being configured. Once observations for a plate are done, the newly configured plate is tumbled into position. The average configuration time for OzDES fields is 40 minutes.

and are used to correct for the wavelength dependent throughput differences between fibres that are not corrected by flap flats. Applying these corrections (often termed an illumination correction) to the flap flats leads to better sky subtraction, especially when the sky background is high due to the presence of the moon. As with Y1, the flap flats are used to determine the location of the fibres on the CCD and to measure the fibre profiles.

For OzDES Y2 and Y3 observations, we also modified the F-star input catalogue. F-stars are used to derive sensitivity functions and to monitor throughput, which mostly depends on seeing and the presence of clouds. They can also be used to define a zero-point that can be used to scale spectra from multiple observations before combining them. Instead of observing stars as faint as $m_r = 20$ mag, as we did in Y1, we restricted the F-stars to the magnitude range $17 < m_r < 18$ mag, as we found that fainter stars were too faint to reliably determine the sensitivity functions and to monitor throughput. The magnitude reported here and throughout the paper is the r-band magnitude² within a 2'' diameter aperture on the DES images. The diameter of the aperture best matches the diameter of the 2dF fibres projected onto the sky.

The observing log for Y2 of OzDES is presented in Table A1, and for Y3 in Table A2. In 2014, OzDES began collaborating with a new AAT observing program 2dFLenS (Blake et al. 2016), which conducted an extragalactic redshift survey of targets that were more than 3 magnitudes brighter than the typical OzDES target. The shorter exposure time needed by 2dFLenS allowed for better allocation of short observing windows around the longer OzDES exposures, as well as more flexibility in scheduling observations at favorable airmasses. Thus a time exchange between the two surveys was employed. It also resulted in a common observing run accounting system (thus yielding non-consecutive run numbers for OzDES observing runs).

Y2 (Y3) of OzDES was allocated 16 (20) nights on the AAT, of which 5.5 (4.4) nights were lost to weather or instrument failure. A further 3.5 (0.7) nights were operational but under adverse weather conditions and were dedicated, in part, to the bright target backup program (see Section 2.3). The remaining 8.0 (14.9) nights were observed under ideal conditions and fully dedicated to the main OzDES program. Y1 had a total of 14 nights, 4.0 of which were lost to weather or instrument failure, with the remainder (10.0 nights) dedicated to the OzDES main program. Further OzDES observing beyond Y3 consists of 20 nights each year on the AAT in the second semesters of 2016 (Y4 – just concluded) and 2017 (Y5), with a final allocation of 12 nights in the second semester of 2018 (Y6).

2.2 Data Reduction

The processing of the raw data is described in detail in Yuan et al. (2015). Here we briefly summarize the main steps. Each observation consists of one or more exposures of the field, an arc frame, and two fibre flats. To get sufficient counts in the fibre flats for both arms, one requires two exposures with different exposure times. The fibre flats are used to locate and trace the spectra on the CCDs (the so-called tram line maps), and the arcs are used to set the wavelength scale.

For each exposure, the overscan region is used to remove the bias, and for data taken with the old blue CCD in Y1 only, bias

² We use the MAG_APER_4 r-band magnitude that is provided by the DES pipeline (Mohr et al. 2012).

Table 1. OzDES fibre allocations by target type for each of the first three years of the survey.

Object Type	Year 1		Year 2		Year 3	
	Fibre Hours	Fraction Fibre Time	Fibre Hours	Fraction Fibre Time	Fibre Hours	Fraction Fibre Time
AGN	9827	38.3%	7602	26.0%	9373	24.9%
Bright Galaxies	28	0.1%	2863	9.8%	1100	2.9%
Cluster Galaxies	854	3.3%	956	3.3%	747	2.0%
ELGs	6175	24.1%	–	–	–	–
LRGs	2539	9.9%	8400	28.6%	9788	26.0%
Photo-z Targets	649	2.5%	668	2.3%	883	2.3%
Radio Galaxies	1409	5.5%	2032	7.0%	2386	6.3%
Strong Lens	45	0.1%	81	0.3%	–	–
SN Hosts	3041	11.9%	6230	21.3%	12600	33.5%
Live Transients	1031	4.0%	494	1.7%	740	2.0%
Total	25598		29326		37617	

and dark frames are used to reduce the impact of cosmetic defects (see Sec. 2.1). The one-dimensional spectra are then extracted using the tram line maps to guide the extraction and then resampled to a common wavelength scale.

An important processing step is the removal of the coherent residuals that remain after subtracting a spectrum of the night sky³ (Sharp & Parkinson 2010). Without this step, the residuals impede the identification of real spectral features.

We used a modified copy of version 6.2 of 2dFDR (Croom et al. 2004) to process the data from AAOmega. Both the data from Y1, which had used an earlier version of 2dFDR, and the data from Y2+Y3 have been processed consistently with the newer version.

The publicly available version of 2dFDR improves on the earlier version of 2dFDR used in Yuan et al. (2015) in a number of ways. Tram line maps (the location of the spectra on the detectors) are more precise, and one can now simultaneously fit a model of the background scattered light together with the flux in the fibres for each column of the detector. The scattered light is modeled with splines and the fibre profiles are modeled with Gaussians. The widths of the Gaussians and their locations are determined from the flat fields.

The publicly available version of 2dFDR was modified in several key areas:

- Using PyCosmic (Husemann et al. 2012) instead of LACosmic (van Dokkum 2001) to locate pixels affected by cosmic rays. These pixels are marked as bad and are removed from further analysis.
- Using singular value decomposition (SVD) when the least-squares solution fails to produce an adequate solution to the matrix equation that is used to optimally extract the flux in the fibres (see Sharp & Birchall 2010, for details). On average, we use SVD instead of least squares once every 200 columns. Without this modification, the data in these columns would have been treated as bad and not used.
- Average over 10 columns when fitting the fibre profile for low signal-to-noise regions in the flat fields. This is most severe in the blue end of the spectral range. This results in more accurate measurement of the fibre profile, which leads to more accurate extraction of the flux from the spectra.

³ The spectrum of the night sky is determined from the 25 sky fibres that are distributed across the 2dF field-of-view.

- Applying an illumination correction to the flap flats using the dome flats, which, as noted above, leads to better sky subtraction.
- Applying a different set of sensitivity functions for the instrument before and after the upgrade of the CCDs.

Once the data from the red and blue arms have been processed with 2dFDR, we merge the red and blue spectra into a single spectrum. Since some targets are observed over multiple nights and can appear in more than one field (because of field overlap) we sum all the data on a single target into one spectrum, first scaling each spectrum (the variance is scaled by the square of this scaling) and then weighting by the inverse of the variance in the sum. We scale the spectrum with either the inverse of the median value of the spectrum or the inverse of 0.1 times the square root of the median of the variance, whichever turns out to be the smallest. This accounts for cases in which the median flux is close to zero, which would result in very large scale factors. The 0.1 factor was chosen after some experimentation. We plan to revisit this choice for the next data release.

While the processing has improved, there is still room for further improvement. In particular, one can sometimes see a discontinuity in the spectra near the wavelength where the dichroic splits the two arms of the spectrograph. This is largely due to errors in sky subtraction and is caused by a combination of a residual background (sometimes caused by the wings of a bright star⁴), and poor spectral uniformity in the flap flats (mostly affects Y1 data when dome flats were not taken). The accuracy of the sky subtraction, which is assessed by examining how well the continuum of the sky is removed from the sky fibres, is about 1% in the best cases and 6% in the worst cases.

We are investigating techniques to further improve the processing. In addition to removing the spectral inhomogeneity in the Y1 flap flats and improving the modeling of the background, we are experimenting with more complex fibre profiles. In detail, the fibre profile is not Gaussian. The core of the profile is more boxy than a Gaussian and there are broad exponential wings. We anticipate that these improvements will be available before the end of OzDES.

⁴ Usually this was unintended. In regions close to stars that are heavily saturated in the DES images, source detection algorithms, such as SExtractor, can erroneously break the image of the star into many false objects. Some of these false objects make it into the source catalogues. The problem mostly affects data from Y1. Greater scrutiny of the input catalogues during Y2 and Y3 largely eliminated this problem.

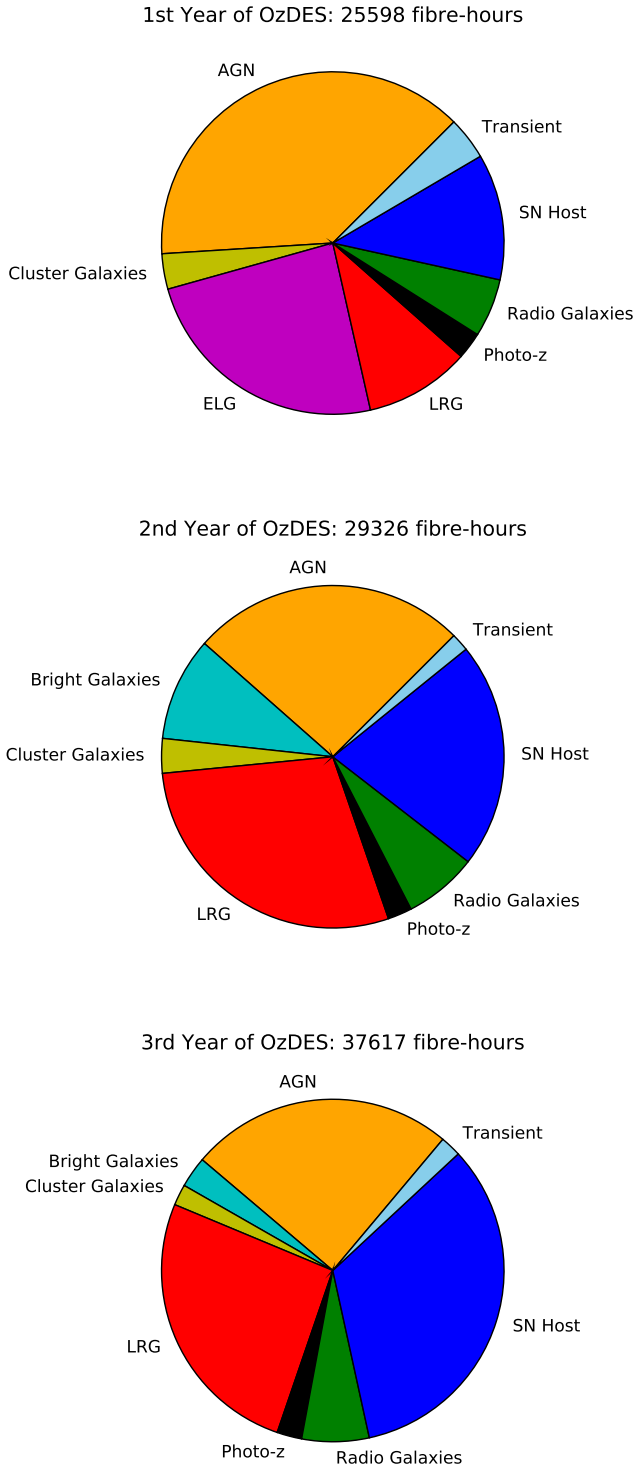


Figure 1. Fibre allocation fraction vs. object type for OzDES Y1, Y2, and Y3. Note the steady increase in the number of SN hosts over the first three years.

2.3 OzDES Target Allocations for Y2 and Y3

The target selection procedure and primary target classes for OzDES were described in detail in Section 3.2 and 3.3 of Yuan et al. (2015), respectively. A number of changes, which are described in detail below, were implemented for Y2+Y3. Fibre observing time allocations for Y1+Y2+Y3 of OzDES are summarised in Table 1, and presented in Figure 1.

The OzDES active galactic nuclei (AGN) reverberation mapping (RM) project (King et al. 2015) transitioned from Y1 operations of identifying AGN suitable for RM followup to Y2 operations of actively monitoring AGN selected in Y1. This decreased the fraction of fibres allocated to AGN, as the Y1 target selection program had concluded. OzDES now has a core sample of 771 AGN that are monitored for the RM program across all 10 DES-SN fields, which should consistently account for 25% of fibre allocations for the remainder of the project.

The allocation of fibres to supernova host-galaxies⁵ nearly doubled from Y1 to Y2, and increased a comparable amount between Y2 and Y3. This is a consequence of both the increase in number of confident prior SN candidates from DES and an extension of the SN host magnitude limit to include fainter hosts (down to $m_r = 24.0$ mag). The increase of DES Y1 SN candidates is partly due to an improved reprocessing of the DES Y1 imaging data (Kessler et al. 2015) yielding several hundred new SN candidates with hosts to be targeted by OzDES.

In the first year of OzDES observing, we found that adverse observing conditions (i.e. poor seeing or significant extinction) resulted in low redshift success rates (of order 10%). Thus at the end of Y1 we implemented a poor weather backup program comprised primarily of a new “bright galaxy” target class, consisting of galaxies with integrated magnitude of $18 \lesssim m_r \lesssim 19.5$ mag identified in DES imaging but not tied to an existing DES spectroscopic followup program. The goal of this program is to maximise the scientific utility of data taken with OzDES even in adverse conditions by expanding the extragalactic redshift catalogues in the DES SN fields, many of which have significant archival imaging data across the electromagnetic spectrum. Such a program will help with photo-z calibration and SN lensing measurements.

The bright program was triggered at the discretion of the observers, and was typically triggered when the seeing was worse than $3''$, or there was significant cloud cover. An important consideration in making the decision to switch to the backup program is the 40-minute configuration time for a 2dF plate, meaning the decision to switch to the bright program would have at least a 40-minute delay before implementation.

OzDES target selection procedures were modified for emission line galaxies (ELGs) and luminous red galaxies (LRGs) in Y2 and Y3. After Y1, it became apparent that we would not be able to obtain 10,000 redshifts for ELGs and 10,000 redshifts for LRGs with the number of spare fibres available during the survey. Therefore, after Y1, ELGs were no longer targeted for photometric redshift training, releasing a large fraction of fibres. Accordingly, the fraction of fibres allocated to LRGs increased, as these LRGs were of equal priority in the target selection algorithm to the ELGs that were removed (see Section 3.2 of Yuan et al. 2015, for details). The follow-up of ELGs in the DES fields was continued at other facilities.

After Y1, OzDES also began targeting galaxies selected with the redMaGiC (Roza et al. 2016) algorithm, which selects LRG

⁵ This includes the hosts of transients that may not be supernovae.

galaxies with accurate and unbiased photometric redshifts. These galaxies are being used in large scale structure and weak lensing studies in DES. RedMaGiC galaxies are counted as LRGs in Table 1 and Fig. 1. We also targeted Brightest Cluster Galaxies (BCGs) from the SpARCS catalogue (Webb et al. 2015), tertiary calibration stars in the DES supernova fields, host-galaxies of exotic transients from SNLS (following Lidman et al. 2013), and faint QSOs in the S1 and S2 fields (those which overlap with SDSS Stripe 82).

Finally, the sample of radio-galaxies in Y2 and Y3 was extended to galaxies with lower radio luminosities. Many of these galaxies tend to be relatively bright nearby star-forming galaxies. This leads to brighter galaxies being targeted in Y2+Y3 than in Y1, as can be seen in the bottom left hand plot of Figure 2.

3 REDSHIFT RESULTS FROM THE FIRST THREE YEARS OF OZDES

3.1 Redshift Outcomes

For Y1 and Y2, redshifts were obtained using the RUNZ redshifting software, which was developed by Will Sutherland for the 2dF Galaxy Redshift Survey. In Y3, we switched to Marz⁶ (Hinton et al. 2016), after first verifying that the redshifts from RUNZ and Marz were the same. Marz is an open-source, client-based, web-application that provides most of the functionalities of RUNZ as well as new features, but none of the difficulties associated with installing and compiling RUNZ.

As for Y1, each source was inspected by two redshifters. A third redshifter inspected their work to resolve conflicting assignments and merge the results.

At the conclusion of Y3, OzDES has obtained spectra for a total of 28,504 targets yielding 17,893 successful redshifts (a successful redshift has $Q \geq 3$, see Section 3.2). Table 2 presents the number of redshifts for each target type at the end of each of the first three years of OzDES. We note that some targets are triggered for spectroscopy by multiple DES science working groups. Over multiple runs, an object that was tagged with a certain type (e.g. Photo-z or ELG) in an earlier run may have been tagged in a later run with another type (e.g. SN host) and reobserved. This is one reason why the number of objects with redshifts can drop from one year to the next, as is the case for ELGs between Y2 and Y3. The number can also change if the data were reprocessed and re-analysed between the OzDES observing seasons.

The number of observing nights increased progressively from Y1 to Y3 (as did the fibre-hours on sky, see Table 1), but the redshift success rate slowed over this period. The change in the redshift success rate is due to an increase in the relative number of fainter objects being targeted, as brighter targets require less exposure time to obtain redshifts and are thus removed from the OzDES target pool earlier.

Figure 2 presents the magnitude distributions of several target classes, separated by redshift status: all targeted objects (open histograms), all objects with secure redshifts for Y1-Y3 combined (filled coloured histograms), and those with redshifts obtained in Y1 of OzDES (filled grey histograms). We also show the redshift completeness versus r-band magnitude for these target classes.

Table 2. OzDES cumulative redshift counts by target type for the first three years of the survey. Not all target types are listed.

Object Type	End Y1 # Redshifts	End Y2 # Redshifts	End Y3 # Redshifts
AGN	1781	1901	1916
Bright Galaxies	24	2183	2902
Cluster Galaxies	284	525	732
ELGs	1293	1429	1419
LRGs	711	2528	4108
Photo-z Targets	1622	1741	1740
Radio Galaxies	143	788	1027
Strong Lenses	3	14	14
SN Hosts	498	1345	2566
Live Transients	232	369	494
Other	47	266	1658
Total	6648	13089	17893

The redshift success rate shows a characteristic trend with magnitude for most target types, where we have a high likelihood of obtaining a redshift for targets brighter than $m_r = 21$ mag in a single observation. As we will show below, this is driven by signal-to-noise. Fainter objects, which continue to be targeted, are steadily accumulating the necessary signal-to-noise to obtain a redshift.

In Fig. 3, we show redshift distributions for the five object classes shown in Fig. 2 as well as for AGN. The SN hosts extend up to $z \sim 1.2$. At this redshift the [OII] $\lambda 3727$ doublet is close to the red end of the spectral range covered by OzDES spectra. In principle, one could push to higher redshifts by changing the wavelength settings of AAOmega, but this comes at the expense of losing coverage in the blue, which would have an impact in the number of redshifts that are obtained for objects at lower redshifts. The AGN sample is intrinsically brighter and thus extends to much higher redshifts – this sample consist of objects that are part of the AGN reverberation mapping programme, additional AGN that were screened during Y1, and faint QSOs that are observed in the S1 and S2 fields.

3.2 Conditions for Redshift Success

We examine the likelihood of securing a redshift, first as a function of signal-to-noise ratio, and then as a function of magnitude. In Sec. 6, we'll use these likelihoods to compute the likely yield of SN host redshifts by the end of the survey.

OzDES assigns a redshift quality flag to each redshift. These values are described in detail in Yuan et al. (2015), but are summarised below:

- $Q = 4$, redshift based on multiple strong spectroscopic features matched, $> 99\%$ confidence.
- $Q = 3$, redshift based typically on a single strong spectroscopic feature or multiple weak features, 95% confidence.
- $Q = 2$, potential redshift associated with typically a single weak feature, low confidence.
- $Q = 1$, no matching features, thus no constraints on redshift.
- $Q = 6$, securely classified star.

In Figure 4, we plot the fraction of targets achieving a given redshift quality Q as a function of the (logarithmic) S/N for spectra. This is plotted for selected object classes, split by the three (extragalactic) Q values. These are calculated as the mean S/N per \AA in the wavelength range $6500 \text{\AA} \leq \lambda \leq 8500 \text{\AA}$, which is redward

⁶ Manual and automatic redshifting software, <http://samreay.github.io/Marz/>

[h]

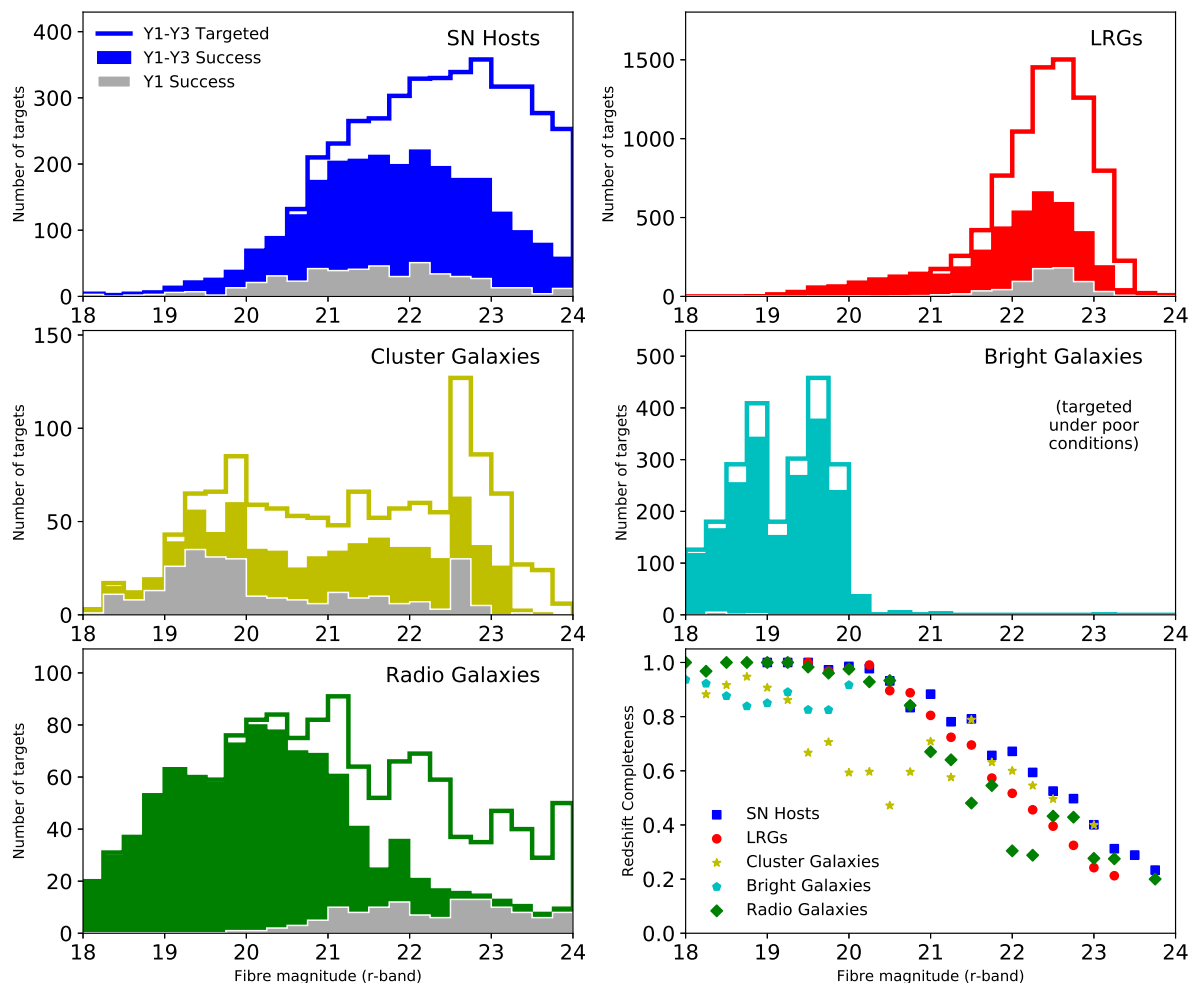


Figure 2. Fibre magnitude distribution of all objects targeted by OzDES from Y1-Y3 (white histogram), objects with successful redshifts at the end of Y3 (filled histogram), and (for comparison) those with successful redshifts at the end of Y1 Yuan et al. (as in Figure 4 from 2015). Histograms for five categories of objects are shown, and in the lower right panel we show the redshift success fraction (number of successful targets divided by full number of targets in each magnitude bin) as a function of magnitude for the five target classes.

of the 4000 \AA break for intermediate redshift ($z \sim 0.5$) galaxies, and is where the throughput of AAOmega is greatest (thus this wavelength range typically dominates whether or not a successful redshift is achieved).

These redshift quality plots show that for most target categories (including those not shown here), the S/N at which the likelihood of securing a redshift ($Q \geq 3$) exceeds 50% is 2 to 3 in 1-\AA bins (i.e. $\log(S/N) \approx 0.3$). The one obvious exception to this trend is ELGs (second column of Figure 4) which have a flatter trend of success versus spectrum S/N – this is because the average spectrum S/N is weakly correlated with the strength of the narrow oxygen doublet responsible for most successful ELG redshifts.

In Fig. 5, we examine how the redshift completeness changes as a function of r-band magnitude. We limit the analysis to SN hosts, as they cover a broad range of magnitudes and galaxy types, and represent the largest source of uniformly selected targets. As expected, redshift completeness increases with exposure

time. We reach a completeness of over 90% for objects down to $m_r = 23.75$ mag, which is the midpoint of the last magnitude bin in Fig. 5. We use Fig. 5 to estimate the yield of SN host galaxies that we expect by the end of Y6 in Sec. 6.

3.3 Redshift Reliability

We now turn the question of how reliable the OzDES redshifts are, particularly for those with a redshift quality flag $Q = 3$, which are nominally expected to be correct 95% of the time. Fortunately, for the SN host galaxies in the OzDES sample, we did not remove these objects from the target queue once they were marked as a $Q = 3$ redshift, but only once a highly secure $Q = 4$ redshift was obtained.

We thus examined the redshift catalogs compiled at the end of each observing run to examine which SN hosts had initially achieved a successful redshift with $Q = 3$ but ultimately succeeded

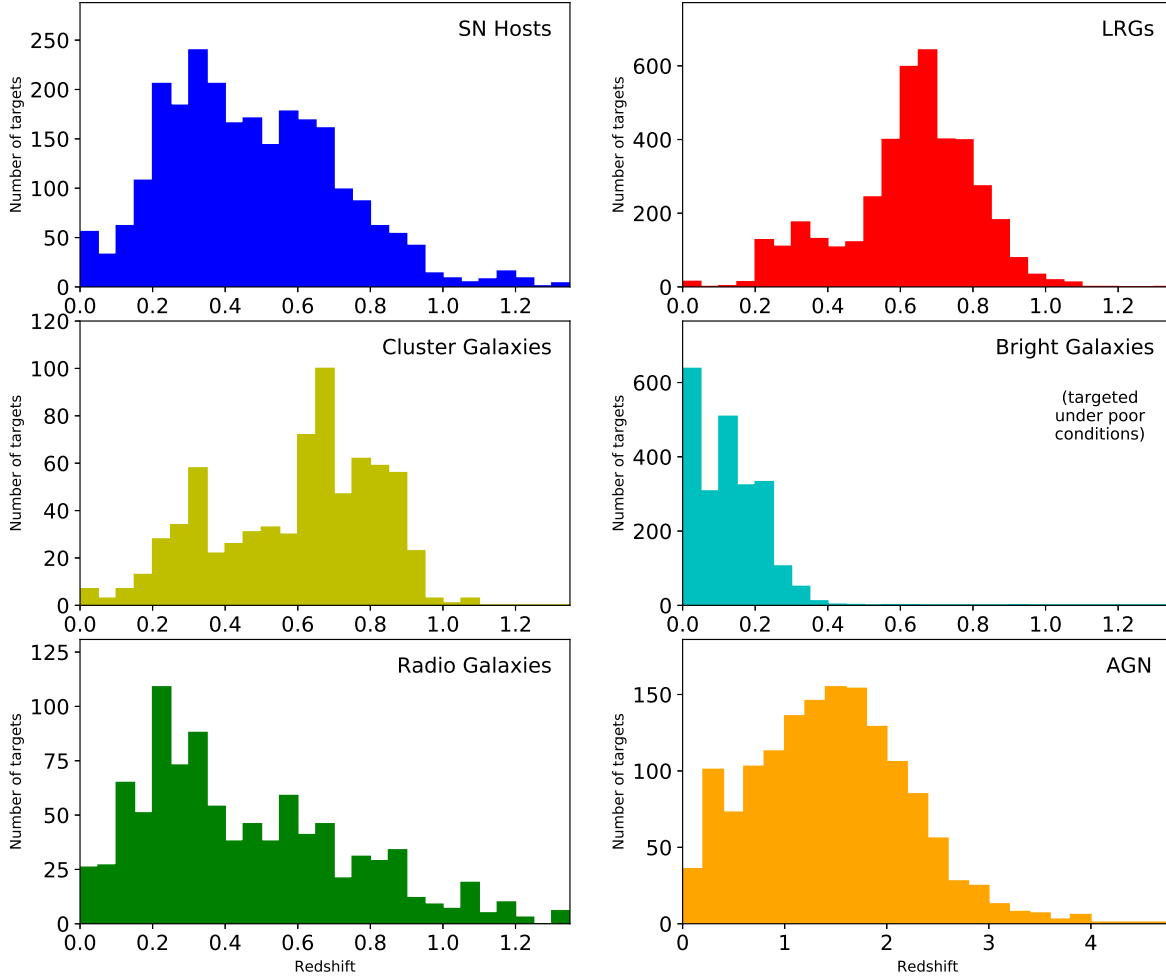


Figure 3. Redshift distributions at the end of Y3 for the 5 different object types shown in Fig. 2. Also shown, in the lower right panel, is the redshift distribution for AGN. Note that the redshift scale of the AGN plot differs from the other plots.

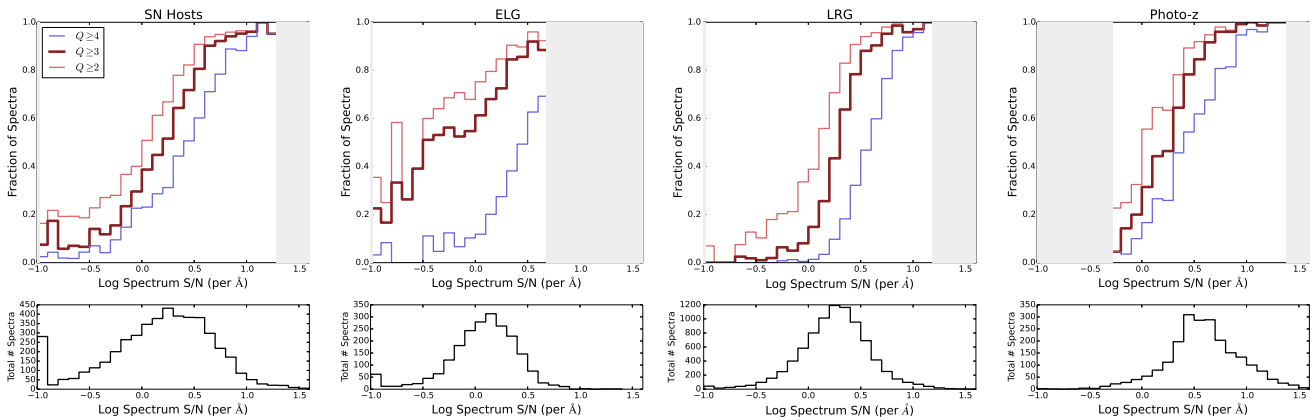


Figure 4. Distributions of spectra signal-to-noise (S/N) for the final redshift quality flag (Q) groups for each type of OzDES target. The top panels show the fraction of targets achieving a quality flag Q as a function of S/N for several target types, while the bottom panels show histograms of the S/N for those same target types. In the upper panels bins with less than 20 total spectra are omitted (denoted by grey shaded areas).

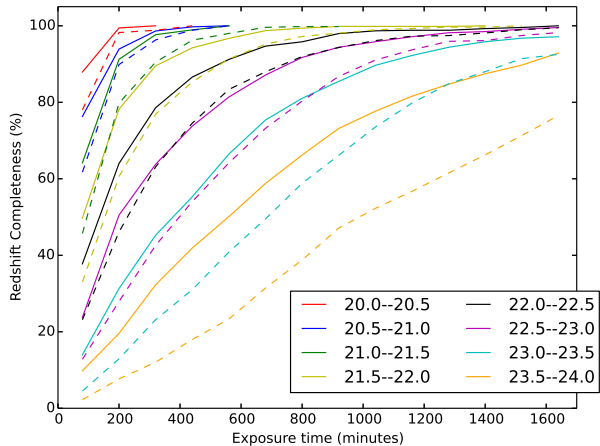


Figure 5. Redshift completeness versus exposure time for different magnitude bins in the SN host sample. For each magnitude bin, a solid line is shown to present all successes ($Q \geq 3$) and a dashed line of the same colour is shown to present the most secure redshifts ($Q \geq 4$). Note how the fraction of sources with a redshift monotonically increases with exposure time for all objects, irrespective of magnitude.

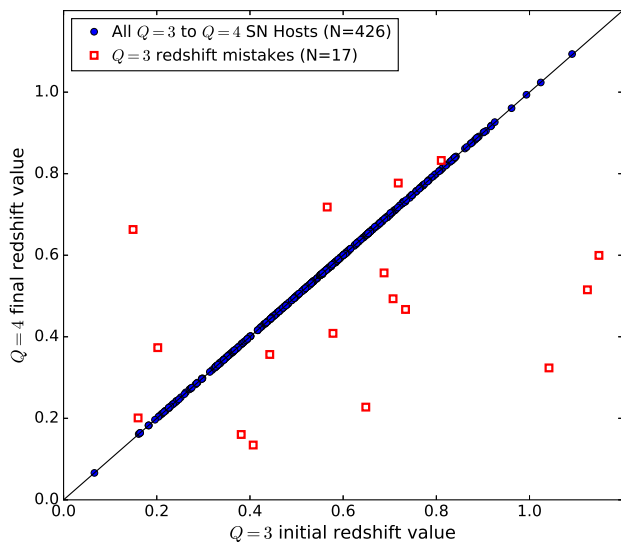


Figure 6. Redshift comparison for OzDES SN hosts with initial redshift quality $Q = 3$ that were successfully re-observed until attaining $Q = 4$. The full sample is shown as small blue dots ($N = 426$ objects) while the ($N = 17$) outliers (defined as $\Delta z > 0.003$) are shown as large red squares.

in achieving a $Q = 4$ redshift. Out of the 2,566 SN hosts with successful redshifts, 426 have a final quality flag of $Q = 4$ but previously had a $Q = 3$ quality flag at the end of a prior run. In Figure 6 we plot the final ($Q = 4$) redshift against the initial ($Q = 3$) redshift for these SN hosts.

We define outliers as those with a redshift change of $\Delta z > 0.003$ (note we obtain the same sample if we define this as $\Delta z / (1+z) > 0.003$). This provides 17 objects (out of 426) whose initial $Q = 3$ redshift was not consistent with its final $Q = 4$ redshift. This yields a redshift error rate of 4% for $Q = 3$ redshifts. Implicit

in this calculation is the assumption of a zero redshift error rate for $Q = 4$ redshifts. Using objects in the overlap regions between DES fields that have been observed more than once, Yuan et al. (2015) found no inconsistent $Q = 4$ redshifts out of 136 objects. Hence, using a zero redshift error rate for objects with $Q = 4$ to derive a redshift error rate of 4% for $Q = 3$ redshifts is reasonable. It is similar to the error rate for $Q = 3$ redshifts found in Yuan et al. (2015). We also note the RMS difference between the $Q = 3$ and $Q = 4$ redshift values is $\sigma_z = 4.2 \times 10^{-4}$, consistent with the galaxy redshift uncertainty reported in (Yuan et al. 2015).

The number of SN hosts with an erroneous redshift will be smaller than 4%, since we only remove SN hosts from the observing queue objects once $Q = 4$. The ratio of the number of SN hosts with a $Q = 3$ redshift to the number of SN hosts with a $Q = 4$ redshift is 1 to 4. Hence the number of SN hosts with an erroneous redshift will be less than 1%. Note this value for redshift reliability is related to redshifts secured for the nominal SN host. The additional error of incorrectly identified hosts (shown in Gupta et al. 2016, to be around 3%) is important for SN Ia cosmological analyses, but it beyond what we examine here.

4 THE FIRST OZDES REDSHIFT RELEASE

This paper marks the first release of data from the OzDES survey, which we henceforth refer to as OzDES-DR1⁷. OzDES-DR1 consists of the redshift catalogue from the first three years of observing, and includes coordinates and redshifts for all target categories in the OzDES program except supernova host galaxies. The redshifts for SN hosts will be published after the OzDES survey ends. OzDES-DR1 includes confident extragalactic redshifts ($Q = 3$ and $Q = 4$), as well as confirmed foreground Milky Way stars ($Q = 6$). In total, this first redshift catalogue contains 14,693 redshifts in the ten DES supernova fields.

OzDES-DR1 also includes the primary target type for each object. We note several important caveats associated with this information. First, some objects were selected for spectroscopic followup by multiple science working groups within the DES collaboration. For practical purposes, OzDES tagged each multiply-requested object by the target category with highest (active) priority for followup (see Section 3.2 and Table 3 of Yuan et al. 2015, for further details on the target categories and priorities). Second, we caution against interpreting the set of objects in a given category as a complete demographic sample. There are two main reasons for this: i) the selection criteria for some target types evolved during the course of the first three years, and ii) objects that were initially included early in the OzDES target list might have been deselected once a redshift became available from a recently published survey (e.g. GAMA or VIPERS).

Objects identified from DES imaging as targets for spectroscopy were first checked against a compilation of redshifts in the DES supernova fields from surveys listed in Table 3, which also lists the target density of these surveys and the median redshift for their targets in the OzDES fields. Each DES science working group would apply different criteria to de-select objects. We note that OzDES has a higher on-sky target density than many wide-area surveys (such as 6dF, 2dFGRS, SDSS) and a similar redshift range to many deep surveys (such as ACES, PRIMUS, VIPERS, VVDS – see Figure 7).

⁷ The redshift catalogue will be made available from the Strasbourg Astronomical Data Center and <http://www.mso.anu.edu.au/ozdes/DR1>

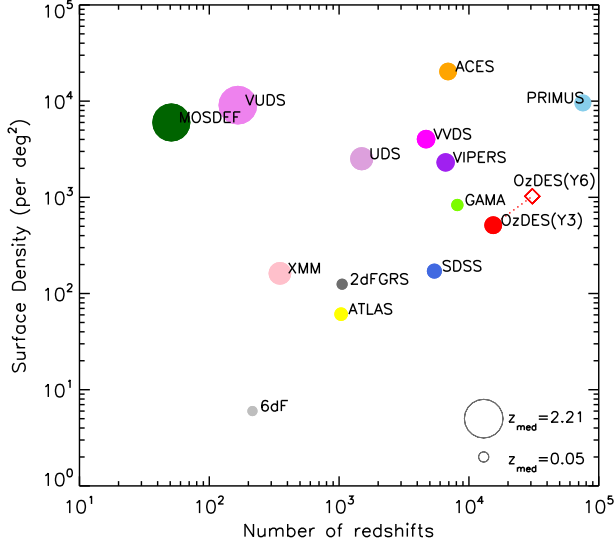


Figure 7. Comparison of OzDES-DR1 against outcomes for other major redshift surveys in the OzDES fields. The average redshift surface density of the survey is plotted against total number of redshifts in the OzDES fields, with the size of each point corresponding to the median redshift of the survey in our fields. OzDES-DR1 represents the second highest number of redshifts produced in these fields, with a surface density approaching that of surveys on larger (8m-class) telescopes. As time progresses, this point will move further up and to the right, as shown by the dotted line.

Table 3. Extragalactic redshift catalogues searched for existing redshifts for DES photometric targets sent to OzDES.

Catalog	# Redshifts in OzDES fields	z_{med}^a	Σ_z^b [deg $^{-2}$]	Ref.
2dFGRS	1055	0.12	125	1
6dF	215	0.05	6	2
ACES	6908	0.62	20320	3
ATLAS	1036	0.31	61	4
GAMA	8143	0.21	832	5
MOSDEF	51	2.17	6000	6
PRIMUS	75511	0.56	9583	7
SDSS	5417	0.42	171	8
UDS	1493	1.03	2518	9
VIPERS	6615	0.67	2307	10
VUDS	166	2.21	9075	11
VVDS	4676	0.69	4025	12
XMM	350	1.00	162	13
OzDES	15388	0.63	513	

^a Median redshift of the surveys' redshifts in the OzDES fields.

^b On-sky redshift density of the (entire) survey.

References: (1) Colless et al. (2001); (2) Jones et al. (2009); (3) Cooper et al. (2012); (4) Mao et al. (2010, 2012); (5) Liske et al. (2015); (6) Kriek et al. (2015); (7) Coil et al. (2011), Cool et al. (2013); (8) Abazajian et al. (2009); (9) Bradshaw et al. (2013), McLure et al. (2013); (10) de la Torre et al. (2013); (11) Tasca et al. (2016); (12) Le Fèvre et al. (2013); (13) Stalin et al. (2010).

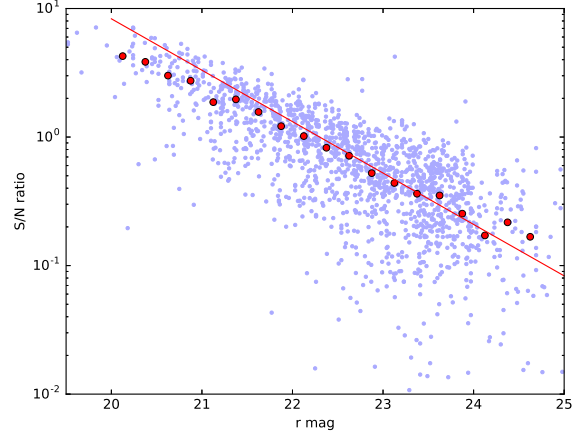


Figure 8. Spectrum signal-to-noise (S/N) ratio of SN hosts in 40 minutes of integration plotted against catalog magnitude. Shown here, as the blue points, are the results for SN hosts that were observed during the second and third years of OzDES. Plotted in red circles are the median values in bins of 0.25 mag. The red line has a slope of -0.4 (the expectation assuming Poisson statistics) and is fixed to $S/N = 2$ at $m_r \sim 21.5$ mag. At bright magnitudes, we expect the red circles to lie below the red line, because of the contribution made by galaxy spectral features to the noise.

5 SIGNAL-TO-NOISE BEHAVIOUR

5.1 Signal-to-noise behaviour with magnitude

In Section 3.2 we showed that, on average, we obtain a $Q \geq 3$ redshift once a S/N of approximately 2 to 3 in a 1-Å bin is reached. Here, we inspect how the S/N varies with target magnitude for a fixed exposure time under uniform observing conditions.

To find frames taken under similar observing conditions, we use the zeropoints for all single 40-minute OzDES exposures taken during Y2 and Y3 (the zeropoints for Y1 are less accurate). These zeropoints were calculated using the F-star catalogs for the DES-SN fields (see Yuan et al. 2015, for details). We select all exposures whose zeropoints are within 0.1 magnitudes of a chosen value⁸, thereby selecting the frames that have been observed under a similar observing conditions. In total, 20 frames were selected. For these exposures we calculate the S/N of the individual object spectra from 6500 to 8500Å and compare them with the object r-band magnitudes in Figure 8.

We limit the analysis to SN hosts, as they cover a broad range of magnitudes and a broad range of galaxy types. LRGs, on the other hand, cover a narrow magnitude range and a narrow range of galaxy types (see Fig. 2).

Figure 8 illustrates that, on average, a S/N of ~ 2 is obtained for SN hosts with $m_r \sim 21.5$ mag in a single 40-minute exposure under the best observing conditions. Hence, from the results presented in Sec. 3.2, we'd expect to obtain redshifts for 50% of sources with $m_r \sim 21.5$ mag in a single exposure.

During a single observing run, most targets are observed with 2 or 3 consecutive 40-minute exposures. Hence, during a single observing run, we'd expect to obtain redshifts for 50% of sources with $m_r \sim 22$ mag. In extrapolating to longer exposures, we have

⁸ The chosen value corresponds to data that were taken during the best 10% of observing conditions.

assumed that S/N increases as $t^{0.5}$. We test this assumption in the next section.

5.2 Signal-to-noise accumulation with repeat exposures

OzDES uses the AAT to routinely obtain redshifts for sources as faint $m_r \sim 24$. Not surprisingly, obtaining redshifts for sources this faint using a 4-m class telescope requires long exposures. Some sources have been exposed for more than a day (1,440 minutes).

These long exposure times give us an opportunity to examine how the signal-to-noise ratio behaves with exposure time for exposure times that are rarely reached for fibre fed spectrographs. With no sources of systematic error, the signal-to-noise ratio should increase as $t^{0.5}$. In OzDES, we compute the average spectrum rather than the sum, so the ideal case is that the noise in the averaged spectrum decreases with the square root of the number of exposures. In this section we examine how close we are to the ideal case.

In Figure 9, we plot how the noise changes with exposure time. We computed the noise over the wavelength range 6610 – 6750 Å which is a region that is relatively free of night sky lines.⁹ Each red line in this figure represents a single object. We exclude F-stars, as the noise may be biased high from real features in the spectra of these bright objects.

In this figure, there are 800 objects, each containing at least 10 good¹⁰ exposures, from the DES C fields, which includes the deep C3 field and the two shallower C1 and C2 fields (See Yuan et al. 2015, for a description of the DES SN fields). Quantitatively similar results are obtained with the other 7 DES SN fields. The horizontal axis represents the number of exposures converted to an exposure time by multiplying the number of exposures by 40 minutes (the exposure time of a single OzDES exposure). The vertical axis has been scaled with respect to the noise in the first exposure – hence all blue curves start with a value of one. As more exposures are added to the averaged spectrum, we expect the curves to trend downwards.

Ideally, the noise in the spectra that go into making the average is the same for all exposures. In practice this is not the case because of variations in seeing and transparency. A natural consequence of these variations is the large scatter in the behaviour of individual objects in the figure. The first exposure might have been taken in good (poor) conditions. If the following exposures were taken in worse (better) conditions, then the curves will not follow the expected trend with the number of exposures, which is represented by the black curve. Thus for this analysis we randomly shuffled the order of the spectra used in the average, and found that this helps to mitigate the impact of this variability but does not eliminate it.

The red circles trace out the median behaviour of the individual blue curves and the solid green line represents the limiting case. The solid black line is a fit¹¹ to the red circles using

$$\frac{n^\alpha + \beta}{1 + \beta} \quad (1)$$

where n is the number of exposures.

For $\alpha < 0$, the expression approaches $\beta/(1+\beta)$ as n becomes large. This represents a lower limit to Eq. 1. The best fit has $\alpha = -0.6$ and $\beta = 0.1$, which places the lower limit at ~ 0.09 . The

⁹ We obtain similar results if we had chosen a region that contains bright night sky lines.

¹⁰ Excludes frames taken when the seeing is worse than 3'' and frames that were taken in cloudy conditions.

¹¹ We include uncertainties when doing the fit, but for clarity, we do not show the error bars in Figure 9

ideal case is represented by $\beta = 0$ and $\alpha = -0.5$. A fit with β set to zero results in $\alpha = -0.48$, which is close to the ideal case, and is closer to the ideal case than what was found in Sharp & Parkinson (2010), who found $\alpha = -0.32$.

We tested the robustness of this result to changes in the analysis. If we used the clipped RMS instead of the normalised median absolute deviation to compute the noise in each spectrum, or if we used the zero-points that were determined from F-stars (see Sec. 2.1) to scale the spectra instead of the median flux of the spectra themselves, we found that our results did not change.

As noted above, $\beta = 0.1$ corresponds to a lower limit of ~ 0.09 . In the ideal case, where there is no lower limit, it would take 120 exposures (or 4,800 minutes) for us to reach this level. Note that none of the objects in Figure 9 have been observed for that many exposures. While one may be tempted to use 120 exposures as the criterion to drop objects, it is likely that OzDES will soon need to stop observing targets for another reason. For SN hosts, we impose a limit of 200 fibres per field per observation in order to achieve the desired overall balance of OzDES science goals (see Yuan et al. 2015, for further details). The other 192 fibres are assigned to other targets. After 3 years of observations, we are beginning to reach this limit for the two DES deep fields (X3 and C3). Once this limit is reached, we will need to start removing objects to allocate fibres for newer targets that have a higher chance of getting a redshift. At the time of writing, the choice of which objects to remove first has not been resolved.

6 FORECASTS FOR OZDES AND FUTURE SURVEYS

We use the results from the first half of the OzDES survey to forecast what will be achieved in the full survey. In this section we will focus on the outcomes for the SN host spectroscopy program within OzDES, since it is the largest source of uniformly selected targets. We estimate the final yield of OzDES SN host redshifts first, and then explore the implications our results have for future multi-object spectroscopy surveys, particularly in the era of LSST.

6.1 Forecast for full OzDES SN host redshift yield

Here we predict the likely yield of the full five-year OzDES program. To aid this analysis, we compile the cumulative number of successful SN host redshifts and the cumulative number of fibre-hours allocated to SN hosts at the end of each observing run. We plot these two quantities in the upper panel of Figure 10. The lower panel of Figure 10 shows the fractions of targets achieving redshift quality Q for each run, with the width of each run equal to the total additional fibre time spent on SN hosts.

These figures show that after the first few observing runs OzDES quickly achieved a relatively constant rate of accumulation of new redshifts, shown as the linear fit which has a slope of 0.1 SN host redshifts per fibre-hour.¹² This is consistent with a steady state of new targets added to the queue, a constant fraction of targets achieving a fully successful $Q = 4$ redshift, and the continued accumulation of S/N for repeat targets.

To calculate the expected SN host redshift yield for the remainder of the survey, we first must predict the likely future fibre

¹² This is equivalent to a 20% success rate per pointing for the default observing strategy of 3×40 minute exposures.

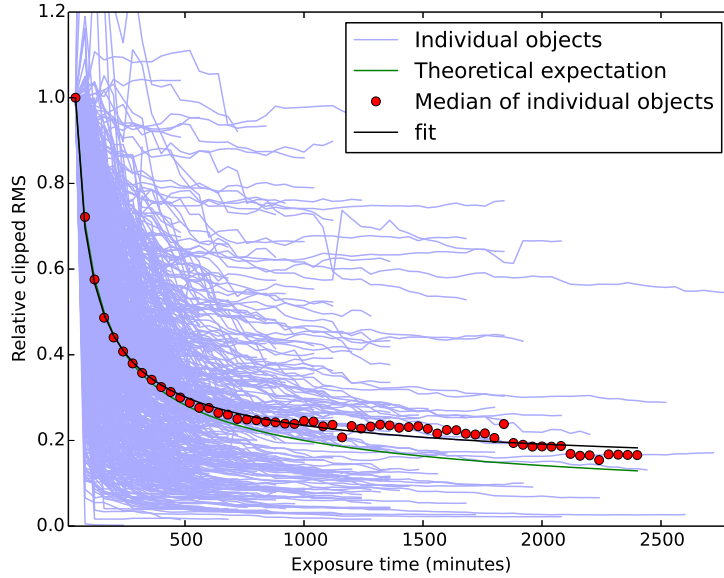


Figure 9. The noise in the averaged spectrum for individual objects (red lines) with multiple exposures as a function of exposure time, normalised to the noise in the first exposure. Also shown are the median values (black circles) compared to the photon-limited noise expectation (black line) which is proportional to $1/\sqrt{t}$. The blue line is a fit to the black points. Note how the blue line sits slightly above the black line. The horizontal axis has been converted from the number of exposures to the total exposure time by multiplying the former by 40 minutes, which is the exposure time for a single exposure.

allocation for SN hosts. In Y1-Y3, OzDES had 48 allocated observing nights plus two additional nights, of which 38.3 nights were clear (76% clear). OzDES accumulated 92,541 fibre-hours over this period, averaging about 2,400 fibre-hours per night. Applying these factors (76% clear nights¹³ at 2400 fibre-hours per night) to the remaining 52 nights allocated to OzDES, we expect around 95,000 fibre-hours remain for the survey. If SN hosts are allocated 40% of the remaining fibre-hours¹⁴, this would result in an allocation of 38,000 fibre-hours to SN hosts in Y4, Y5 and Y6 of OzDES.

If we apply the steady-state accumulation rate of 0.1 redshifts per fibre hour to the remaining fibre-hours in the full OzDES survey, then we would expect an additional 3,800 SN host redshifts. With the 2,566 SN host redshifts already obtained, the final yield would be approximately 6,300 redshifts. However, this is an upper limit. As noted in Section 5.2, we are already approaching the limit of 200 SNe hosts per field for the two deep SN fields C3 and X3, so in the last three years of the OzDES survey, we may need to remove SN hosts for which we have been unable to get a redshift, even after 30 hours of integration.

A more detailed simulation, which includes removing targets from the queue after they have been observed for 30 hours (1800 minutes), irrespective of their status, and includes the probability of obtaining a redshift as a function of exposure time (see Fig. 5), results in a yield of 5,700 SN host redshifts. This is our current best estimate, but it depends on the number of clear nights we obtain during the second half of the survey.

¹³ For Y4, which was in progress as this paper was being written, the clear fraction is approximately 75%.

¹⁴ This is consistent with the fraction of fibres that are allocated to SN hosts during the first part of Y4.

6.2 Insights for future MOS surveys

Finally, we turn to the prospects for future MOS surveys in light of the insights gained from the first three years of OzDES. Here, we will focus on future MOS facilities that are capable of devoting some portion of their fibres toward the observation of supernova host-galaxies, particularly for SNe discovered by the Large Synoptic Survey Telescope (LSST). We will analyse the potential role these facilities could play in a parallel role for LSST as that served by OzDES for DES: classifying live transients and acquiring host-galaxy redshifts for photometric SN classification.

We will primarily focus on three future facilities: the 4-metre Multi-Object Spectroscopic Telescope (4MOST; de Jong et al. 2012), the Subaru Prime Focus Spectrograph (PFS; Sugai et al. 2012; Takada et al. 2014), and the Maunakea Spectroscopic Explorer (MSE; Simons et al. 2014; McConnachie et al. 2014). Numerous other facilities, both in existence and planned for future construction, have MOS capability and will conduct MOS surveys in the LSST era (see McConnachie et al. 2014, for a summary). These include DESI (Levi et al. 2013), which will focus on obtaining galaxy redshifts for Baryon Acoustic Oscillation (BAO) science, WEAVE (Dalton et al. 2012), which will focus on followup of Gaia stars and LOFAR radio galaxies, and MANIFEST (Lawrence et al. 2016) on the Giant Magellan Telescope.

We summarise the key properties of these three facilities in Table 4. 4MOST has similar characteristics to AAOmega in terms of wavelength coverage and telescope aperture. The ratio of the fibre size to average site seeing is also similar. For point sources, the gain from the combination of better seeing and smaller fibre size is as large as the gain one obtains from a larger telescope aperture. For constant fibre size and constant seeing, the signal-to-noise ratio goes as the aperture of the telescope under background-limited conditions. For constant aperture and a constant ratio between fibre

Table 4. Properties of select current and forthcoming MOS facilities.

Facility	AAT	4MOST*	PFS#	MSE†
- Aperture	3.9m	4.1m	8.2m	11.25m
- Field of View	3.4 deg ²	4.1 deg ²	1.25 deg ²	1.5 deg ²
<i>(Low-Res.) Spectrograph</i>				
- Resolution	1800	4000-7800	2300-5000	2500-3000
- Wavelength Range (Å)	3800-8900	3700-9500	3800-12600	3600-18000
- Fibre Diameter	2.0''	1.45''	1.1''	1.2''
- Fibre Multiplex	400	1624	2394	3200

*for the Low Resolution Spectrograph, from <https://www.4most.eu/cms/facility/>

Takada et al. (2014)

† http://mse.cfht.hawaii.edu/docs/mse-science-docs/DSC/MSE.Precis_v8.pdf

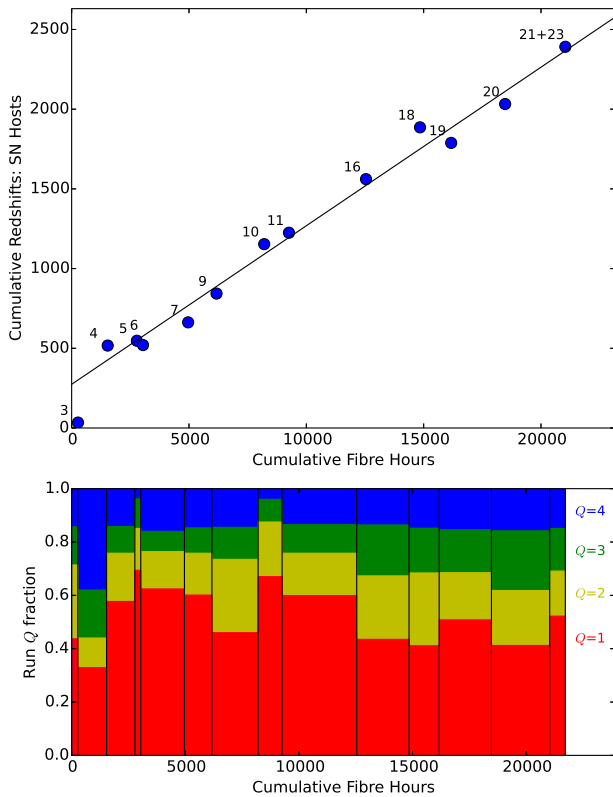


Figure 10. Top: Cumulative redshifts versus fibre-hours at the end of each OzDES run for SN hosts. Points are labeled according to the OzDES observing run number. The first two OzDES runs coincided with the science verification phase of DES, and are not included here. Bottom: Fraction of observed targets achieving a redshift quality Q for the same runs.

size and site seeing, the signal-to-noise ratio for point sources goes as the inverse of the diameter of the fibre. For extended sources, the improvement will be slower. Computing the signal-to-noise ratio for extended sources requires an accurate model of the size distribution of SN host-galaxies. This is beyond the scope of the current paper, and we leave this to future work.

We expect 4MOST on VISTA will be a factor of two faster than AAOmega on the AAT at obtaining the redshift of the same object, with potential added benefits that come from higher spectral resolution, which reduces the impact from night sky lines at red wavelengths, and broader wavelength coverage. Similarly, we

expect that PFS and MSE will be 15 and 23 times faster than AAOmega, respectively. Ignored in these comparisons are differences in instrument throughput, which one might expect to be better for future instruments.

Taking into account the patrol area of these instruments, the area these instruments will be able to cover in the same amount of observing time will be 2.4, 5.2 and 10 times that of the AAT, for 4MOST, PFS, and MSE, respectively.

In computing the likely number of host-galaxy redshifts from these surveys, one needs to make assumptions about the observing strategies of the MOS surveys, and the observing strategy of LSST. Under the assumption that the observing strategies of the MOS surveys are the same as OzDES and that the distribution of SN host-galaxy magnitudes from LSST is the same as DES¹⁵, then for a SN host-galaxy survey with 4MOST using 60,000 fibre-hours (the same number of hours OzDES will spend on hosts by the end of its survey), we would expect a yield of the order 14,000 SN host-galaxy redshifts, which is almost a factor of two larger than the expected yield from OzDES. For PSF and MSE, the numbers of redshifts are 30,000 and 57,000, respectively. Here the increase comes from being able to cover a larger area of the sky in the same observing time.

Not all supernovae with a host redshift will be placed on the Hubble diagram and used in fitting the cosmology. At the end of 3yrs, approximately 40% of DES supernova with a host redshift remain after light curve sampling and light curve quality cuts are applied. Assuming that a similar fraction are kept in future surveys, one can expect a yield of 5,600, 12,000 and 23,000 SNe Ia for 4MOST, PSF, and MSE, respectively.

However, the number of SNe Ia will be further constrained by the observing strategy of LSST. Similarly to DES, LSST will observe a number of deep fields (LSST Science Collaboration et al. 2009b). In one realisation of the LSST survey, approximately 1,500 SNe Ia with light curves of sufficient quality in at least three filters will be obtained per year from 10 LSST deep fields. Over the 10 years that LSST will run, this comes to 15,000 SNe Ia. This then limits the number of SNe Ia that can be placed on the Hubble diagram from an OzDES-sized survey using MSE.

As further details on the observing strategies of LSST and future MOS facilities emerge, the results from OzDES will make it possible to provide more precise estimates of the yields of these upcoming facilities.

¹⁵ The redshift distribution of SNe from DES and LSST are broadly comparable (cf. Fig. 3 with Fig. 11.1 in LSST Science Collaboration et al. 2009b).

7 CONCLUSIONS

In this work, we presented the results of the first three years of OzDES, a spectroscopic survey obtaining redshifts in the 10 DES SN fields. Over 52 observing nights on the AAT, OzDES has obtained 17,893 redshifts in the DES supernova fields. These include a wide variety of targets, such as supernova host-galaxies, AGN, LRGs, radio galaxies, and numerous photometric redshift training samples. At the same time, OzDES has spectroscopically confirmed almost 100 SNe. This work also marks the first OzDES data release (OzDES-DR1), which sees the release of 14,693 redshifts (we note that the SN host redshifts will be released in a future DES analysis).

We examined the requirements for obtaining a redshift in the OzDES data. For nearly all target types (excepting only emission line galaxies), we obtain a redshift for 50% of sources that have a signal-to-noise of 2 to 3 in bins of 1 Å in the red part of the spectrum (observer frame 6,500-8,500 Å).

We also examined the behaviour of the signal-to-noise ratio with exposure time, finding that the change in the signal-to-noise ratio with exposure time closely matches the Poisson limit for exposures as long as 10 hours, which is a measure of how well we control systematic errors in the data processing. However, for longer exposures, the signal-to-noise starts to depart from the Poisson limit.

We use these results to estimate the redshift yields for the remainder of the OzDES survey or other similar future surveys. With the proviso that observing conditions will be similar to what we've experienced so far, we predict a final yield of 5,700 SN host redshifts.

Acknowledgements: This research was conducted by the Australian Research Council Centre of Excellence for All-sky Astrophysics (CAASTRO), through project number CE110001020. BPS acknowledges support from the Australian Research Council Laureate Fellowship Grant FL0992131. R.J.F. is supported in part by fellowships from the Alfred P. Sloan Foundation and the David and Lucile Packard Foundation. Based in part on data collected at the Australian Astronomical Observatory, through program A/2013B/012. This research has made use of the NASA/IPAC Extragalactic Database (NED) which is operated by the Jet Propulsion Laboratory, California Institute of Technology, under contract with the National Aeronautics and Space Administration. This research has made use of NASA's Astrophysics Data System (ADS). We thank the anonymous referee for very helpful feedback which improved the quality of this paper.

Funding for the DES Projects has been provided by the U.S. Department of Energy, the U.S. National Science Foundation, the Ministry of Science and Education of Spain, the Science and Technology Facilities Council of the United Kingdom, the Higher Education Funding Council for England, the National Center for Supercomputing Applications at the University of Illinois at Urbana-Champaign, the Kavli Institute of Cosmological Physics at the University of Chicago, the Center for Cosmology and Astro-Particle Physics at the Ohio State University, the Mitchell Institute for Fundamental Physics and Astronomy at Texas A&M University, Financiadora de Estudos e Projetos, Fundação Carlos Chagas Filho de Amparo à Pesquisa do Estado do Rio de Janeiro, Conselho Nacional de Desenvolvimento Científico e Tecnológico and the Ministério da Ciência, Tecnologia e Inovação, the Deutsche Forschungsgemeinschaft and the Collaborating Institutions in the Dark Energy Survey.

The Collaborating Institutions are Argonne National Laboratory, the University of California at Santa Cruz, the University of Cambridge, Centro de Investigaciones Energéticas, Medioambientales y Tecnológicas-Madrid, the University of Chicago, University College London, the DES-Brazil Consortium, the University of Edinburgh, the Eidgenössische Technische Hochschule (ETH) Zürich, Fermi National Accelerator Laboratory, the University of Illinois at Urbana-Champaign, the Institut de Ciències de l'Espai (IEEC/CSIC), the Institut de Física d'Altes Energies, Lawrence Berkeley National Laboratory, the Ludwig-Maximilians Universität München and the associated Excellence Cluster Universe, the University of Michigan, the National Optical Astronomy Observatory, the University of Nottingham, The Ohio State University, the University of Pennsylvania, the University of Portsmouth, SLAC National Accelerator Laboratory, Stanford University, the University of Sussex, Texas A&M University, and the OzDES Membership Consortium.

The DES data management system is supported by the National Science Foundation under Grant Number AST-1138766. The DES participants from Spanish institutions are partially supported by MINECO under grants AYA2015-71825, ESP2015-88861, FPA2015-68048, SEV-2012-0234, SEV-2012-0249, and MDM-2015-0509, some of which include ERDF funds from the European Union. IFAE is partially funded by the CERCA program of the Generalitat de Catalunya.

REFERENCES

- Abazajian, K. N., et al. 2009, *ApJS*, 182, 543
 Aghamousa, A., et al. 2016, *ArXiv e-print* 1611.00036
 Banerji, M., et al. 2015, *MNRAS*, 446, 2523
 Bazin, G., et al. 2011, *A&A*, 534, A43
 Bentz, M. C., et al. 2009, *ApJ*, 705, 199
 Blake, C., et al. 2016, *MNRAS*, 462, 4240
 Bonnett, C., et al. 2016, *PhysRevD*, 94, 042005
 Bradshaw, E. J., et al. 2013, *MNRAS*, 433, 194
 Brough, S., Green, A., & Bryant, J. 2014, *AAO Observer*, 126, 15
 Campbell, H., et al. 2013, *ApJ*, 763, 88
 Cannon, R., et al. 2006, *MNRAS*, 372, 425
 Coil, A. L., et al. 2011, *ApJ*, 741, 8
 Colless, M., et al. 2001, *MNRAS*, 328, 1039
 Cool, R. J., et al. 2013, *ApJ*, 767, 118
 Cooper, M. C., et al. 2012, *MNRAS*, 425, 2116
 Croom, S., Saunders, W., & Heald, R. 2004, *Anglo-Australian Observatory Epping Newsletter*, 106, 12
 Dalton, G., et al. 2012, in *Proc. SPIE*, Vol. 8446, Ground-based and Airborne Instrumentation for Astronomy IV, 84460P
 Dawson, K. S., et al. 2013, *AJ*, 145, 10
 de Jong, R. S., et al. 2012, in *Proc. SPIE*, Vol. 8446, Ground-based and Airborne Instrumentation for Astronomy IV, 84460T
 de la Torre, S., et al. 2013, *A&A*, 557, A54
 De Silva, G. M., et al. 2015, *MNRAS*, 449, 2604
 Drinkwater, M. J., et al. 2010, *MNRAS*, 401, 1429
 Driver, S. P., et al. 2011, *MNRAS*, 413, 971
 Flaughner, B. 2005, *International Journal of Modern Physics A*, 20, 3121
 Flaughner, B., et al. 2015, *AJ*, 150, 150
 Gupta, R. R., et al. 2016, *AJ*, 152, 154
 Hinton, S. R., Davis, T. M., Lidman, C., Glazebrook, K., & Lewis, G. F. 2016, *Astronomy and Computing*, 15, 61

- Husemann, B., Kamann, S., Sandin, C., Sánchez, S. F., García-Benito, R., & Mast, D. 2012, *A&A*, 545, A137
- Jones, D. H., et al. 2009, *MNRAS*, 399, 683
- Kessler, R., et al. 2015, *AJ*, 150, 172
- King, A. L., Davis, T. M., Denney, K. D., Vestergaard, M., & Watson, D. 2014, *MNRAS*, 441, 3454
- King, A. L., et al. 2015, *MNRAS*, 453, 1701
- Kriek, M., et al. 2015, *ApJS*, 218, 15
- Lawrence, J. S., et al. 2016, in *Proc. SPIE*, Vol. 9908, Society of Photo-Optical Instrumentation Engineers (SPIE) Conference Series, 99089O
- Le Fèvre, O., et al. 2013, *A&A*, 559, A14
- Levi, M., et al. 2013, *ArXiv e-print* 1308.0847
- Lidman, C., et al. 2013, *PASA*, 30, e001
- Liske, J., et al. 2015, *MNRAS*, 452, 2087
- LSST Science Collaboration et al. 2009a, *ArXiv e-prints* —. 2009b, *ArXiv e-print* 0912.0201
- Mao, M. Y., Sharp, R., Saikia, D. J., Norris, R. P., Johnston-Hollitt, M., Middelberg, E., & Lovell, J. E. J. 2010, *MNRAS*, 406, 2578
- Mao, M. Y., et al. 2012, *MNRAS*, 426, 3334
- McConnachie, A., Murowinski, R., Salmon, D., Simons, D., & Côté, P. 2014, in *Proc. SPIE*, Vol. 9145, *Ground-based and Airborne Telescopes V*, 914519
- McLure, R. J., et al. 2013, *MNRAS*, 428, 1088
- Mohr, J. J., et al. 2012, in *Society of Photo-Optical Instrumentation Engineers (SPIE) Conference Series*, Vol. 8451, *Society of Photo-Optical Instrumentation Engineers (SPIE) Conference Series*
- Mudd, D., et al. 2016, *ArXiv e-print* 1606.02717
- Rozo, E., et al. 2016, *MNRAS*, 461, 1431
- Rykoff, E. S., et al. 2016, *ApJS*, 224, 1
- Sánchez, C., et al. 2014, *MNRAS*, 445, 1482
- Scodreggio, M., et al. 2016, *ArXiv e-print* 1611.07048
- Sharp, R., & Birchall, M. N. 2010, *PASA*, 27, 91
- Sharp, R., & Parkinson, H. 2010, *MNRAS*, 408, 2495
- Simons, D. A., Crampton, D., Côté, P., McConnachie, A., Szeto, K., Salmon, D., Devost, D., & Murowinski, R. 2014, in *Proc. SPIE*, Vol. 9145, *Ground-based and Airborne Telescopes V*, 914515
- Stalin, C. S., Petitjean, P., Srianand, R., Fox, A. J., Coppolani, F., & Schwobe, A. 2010, *MNRAS*, 401, 294
- Sugai, H., et al. 2012, in *Proc. SPIE*, Vol. 8446, *Ground-based and Airborne Instrumentation for Astronomy IV*, 84460Y
- Takada, M., et al. 2014, *PASJ*, 66, R1
- Tasca, L. A. M., et al. 2016, *ArXiv e-print* 1602.01842
- Tie, S. S., et al. 2017, *AJ*, 153, 107
- Tyson, J. A. 2002, in *Proc. SPIE*, Vol. 4836, *Survey and Other Telescope Technologies and Discoveries*, ed. J. A. Tyson & S. Wolff, 10–20
- van Dokkum, P. G. 2001, *PASP*, 113, 1420
- Watson, D., Denney, K. D., Vestergaard, M., & Davis, T. M. 2011, *ApJL*, 740, L49
- Webb, T. M. A., et al. 2015, *ApJ*, 814, 96
- York, D. G., et al. 2000, *AJ*, 120, 1579
- Yuan, F., et al. 2015, *MNRAS*, 452, 3047

APPENDIX A: OBSERVING LOGS

The observing runs logs for OzDES Y2 and Y3 are presented below.

Table A1. OzDES second year (Y2) observing log for DES SN fields (c.f. Table 2 of Yuan et al. 2015).

UT Date	Observing Run ^a	Total exposure time for DES field (minutes)										Notes for entire run
		E1	E2	S1	S2	C1	C2	C3(deep)	X1	X2	X3(deep)	
2014-09-17	007	120	120	–	–	–	–	110	–	–	120	Half night lost to weather.
2014-09-18		120	–	–	120	–	–	–	–	120	–	
2014-09-19		–	120	120	40	–	–	–	120	–	–	
2014-09-20		160	–	–	–	–	120	–	–	–	120	
2014-09-21		60*	50*	80	–	160	–	–	–	–	–	
2014-10-27	009	–	–	–	–	75*	75*	50*	–	–	75*	Half night lost to instrument error.
2014-10-28		90	90	–	–	–	–	–	–	90	90	
2014-10-29		–	–	–	–	–	70	90	–	–	–	
2014-10-30		–	–	–	–	90	–	–	90	–	–	
2014-11-18	010	–	120	–	–	–	–	120	–	–	120	Half night lost to weather.
2014-11-19		120	–	–	–	80	90	–	120	–	–	
2014-11-20		–	–	40*	80*	–	–	–	–	80*	–	
2014-11-21		–	–	120	–	–	–	80	–	120	–	
2014-11-27		–	–	–	–	–	–	–	–	–	80	
2014-12-21	011	–	–	–	–	40*	–	120*	–	–	80	Four nights lost to weather
2014-12-22		–	–	–	–	–	–	–	–	–	–	
2014-12-23		–	–	–	–	–	–	–	–	–	–	
2014-12-24		–	–	–	–	90	80	–	–	–	120	
2014-12-25		–	–	–	–	–	–	–	–	–	–	
2014-12-26		80*	–	–	–	–	–	–	–	–	–	
2014-12-29		–	80	–	–	80	–	–	–	–	–	
2014-12-30		80	–	–	–	–	–	–	–	–	–	
2014 (All Y2)		Total (min)	690	530	320	160	500	360	400	330	330	

^aRun numbering includes runs from 2dFLenS project, so is not necessarily contiguous.

* Bright object backup programme for poor conditions, not counted toward final total.

Table A2. OzDES third year (Y3) observing log for DES SN fields (c.f. Table 2 of Yuan et al. 2015).

UT Date	Observing Run ^a	Total exposure time for DES field (minutes)									Notes for entire run	
		E1	E2	S1	S2	C1	C2	C3(deep)	X1	X2		X3(deep)
2015-08-07	016	40	–	–	–	–	–	90	–	–	–	3.5/4.0 clear nights
2015-08-08		80	–	–	–	–	–	60	–	–	–	
2015-08-09		–	120	–	–	–	–	80	–	–	120	
2015-08-10		120	–	–	–	120	–	–	–	80	–	
2015-08-11		–	120	130	–	–	–	80	–	–	–	
2015-08-18		120	–	–	70	–	–	–	80	–	–	
2015-09-16	018	80	80	–	–	–	70	80*	–	–	50	4.0/4.5 clear nights
2015-09-17		80	40	–	–	–	40	50	–	–	80	
2015-09-18		–	–	–	–	110	–	–	80	120	–	
2015-09-19		120	–	80	90	–	–	–	–	–	80	
2015-09-20		–	70*	80	–	–	–	80	80	–	–	
2015-09-21		10*	–	–	90	–	–	–	–	70*	–	
2015-10-10	019	80	80	–	–	–	–	80	–	–	120	2.5/4.0 clear nights
2015-10-11		80	80	–	–	–	–	–	40	–	–	
2015-10-12		–	–	–	–	–	–	–	–	–	–	
2015-10-13		80	80	80	–	–	–	80	120	–	–	
2015-11-12	020	–	–	–	–	50*	–	100	–	–	–	3.0/4.0 clear nights
2015-11-13		–	–	–	–	–	140	80	–	–	–	
2015-11-14		80	–	–	–	–	–	–	–	–	120	
2015-11-15		–	40	–	–	100	–	–	120	120	–	
2015-12-03	021	–	–	120	120	–	–	–	–	–	–	3.1/4.0 clear nights
2015-12-04		–	–	–	–	–	–	–	–	–	60	
2015-12-12		–	80	–	–	–	–	120	–	–	120	
2015-12-13		80	–	–	–	120	–	–	80	–	–	
2015-12-14		–	80	–	–	–	80	–	–	120	–	
2015-12-15		–	–	–	–	–	–	–	–	–	–	
2016-02-06	023	–	–	–	–	–	–	110	–	–	–	0.7/0.7 clear nights
2016-02-07		–	–	–	–	–	120	–	–	–	–	
2015 (All Y3)	Total (min)	920	800	490	370	450	530	930	600	440	750	

^aRun numbering includes runs from 2dFLenS project, so is not necessarily contiguous.

* Bright object backup programme for poor conditions, not counted toward final total.